Journal of Alloys and Compounds 706 (2017) 358–369

Contents lists available at ScienceDirect

Journal of Alloys and Compounds

journal homepage: http://www.elsevier.com/locate/jalcom

Effect of cation vacancies on the crystal structure and luminescent properties of $Ca_{0.85-1.5x}Gd_xEu_{0.1}\square_{0.05+0.5x}WO_4$ ($0 \leq x \leq 0.567$) scheelite-based red phosphors

Dmitry Batuk [a, *], Maria Batuk [a], Vladimir A. Morozov [a, b], Katrien W. Meert [c, d], Philippe F. Smet [c, d], Dirk Poelman [c, d], Artem M. Abakumov [e, a], Joke Hadermann [a]

[a] EMAT, University of Antwerp, Groenenborgerlaan 171, B-2020 Antwerp, Belgium
[b] Chemistry Department, Moscow State University, 119991 Moscow, Russia
[c] LumiLab, Department of Solid State Sciences, Ghent University, B-9000 Ghent, Belgium
[d] Center for Nano- and Biophotonics (NB-Photonics), Ghent University, B-9000 Ghent, Belgium
[e] Center for Electrochemical Energy Storage, Skolkovo Institute of Science and Technology, 143026 Moscow, Russia

Effect of cation vacancies on the crystal structure and luminescent properties of $Ca_{0.85-1.5x}Gd_xEu_{0.1}\square_{0.05+0.5x}WO_4$ ($0 \leq x \leq 0.567$) scheelite-based red phosphors

Dmitry Batuk,[a,*] Maria Batuk,[a] Vladimir A. Morozov,[a,b] Katrien W. Meert,[c,d] Philippe F. Smet,[c,d] Dirk Poelman,[c,d] Artem M. Abakumov,[e,a] Joke Hadermann[a]

[a] EMAT, University of Antwerp, Groenenborgerlaan 171, B-2020 Antwerp, Belgium.

[b] Chemistry Department, Moscow State University, 119991 Moscow, Russia.

[c] LumiLab, Department of Solid State Sciences, Ghent University, B-9000 Ghent, Belgium.

[d] Center for Nano- and Biophotonics (NB-Photonics), Ghent University, B-9000 Ghent, Belgium.

[e] Center for Electrochemical Energy Storage, Skolkovo Institute of Science and Technology, 143026 Moscow, Russia

*Corresponding author. E-mail: dmitry.batuk@uantwerpen.be; Tel. +32 32653305.

Abstract

The $Ca_{0.85-1.5x}Gd_xEu_{0.1}\square_{0.05+0.5x}WO_4$ ($0 \leq x \leq 0.567$) series of cation-deficient scheelites is investigated to unveil the influence of the cation vacancies on the crystal structure and luminescent properties. The concentration of the vacancies is varied by the heterovalent substitution of Gd^{3+} for Ca^{2+}, keeping the concentration of the Eu^{3+} luminescent centers constant in all compounds of the series. The crystal structure of the materials is studied using a combination of transmission electron microscopy and synchrotron X-ray powder diffraction. At low vacancy concentration (x = 0.1, 0.2), cations and cation vacancies are randomly distributed in the structure, and the materials preserve the $I4_1/a$ symmetry of the parent scheelite structure [x = 0.1: a = 5.25151(1) Å, c = 11.39479(2) Å; x = 0.2: a = 5.25042(1) Å, c =

11.41335(2) Å]. At higher concentration, the cation-vacancy ordering gives rise to incommensurately modulated structures. The x = 0.3 structure has a (3+2)D tetragonal symmetry [superspace group $I4_1/a(\alpha,\beta,0)00(-\beta,\alpha,0)00$, a = 5.24700(1) Å, c = 11.45514(3) Å, $\mathbf{q_1}$ = 0.51637(14)**a*** + 0.80761(13)**b***, $\mathbf{q_2}$ = 0.80761(13)**a*** + 0.51637(14)**b***]. At x = 0.4, the scheelite basic cell undergoes a monoclinic distortion with the formation of the (3+1)D structure [superspace group $I2/b(\alpha,\beta,0)00$, a = 5.23757(1) Å, b = 5.25035(1) Å, c = 11.45750(2) Å, γ = 90.5120(2)°, Å, $\mathbf{q}$ = 0.54206(8)**a*** + 0.79330(8)**b***]. In both structures, the antiphase Ca and (Gd,Eu) occupancy modulations indicate that the ordering between the A cations and vacancies also induces partial Ca/(Gd,Eu) cation ordering. Further increase of the Gd^{3+} content up to x = 0.567 leads to the formation of a monoclinic phase (space group $C2/c$) with the $Eu_{2/3}WO_4$-type structure. Despite the difference in the cation-vacancy ordering patterns, all materials in the series demonstrate very similar quantum efficiency and luminescence decay lifetimes. However, the difference in the local coordination environment of the A cation species noticeably affects the line width and the multiplet splitting of the $4f^6$-$4f^6$ transitions.

Keywords

Rare earth; Oxide; Transmission electron microscopy; Diffraction; Luminescence

1. Introduction

The basic scheelite structure has composition ABO_4 ($CaWO_4$) and a tetragonal symmetry (space group $I4_1/a$). It is based on a framework of corner sharing AO_8 and BO_4 polyhedra. The structure can accommodate a variety of chemical species in both A- and B- cation sublattices, which gives rise to a plethora of different compounds with a general composition $(A',A'')_a[(B',B'')O_4]_b$, where A', A'' can be alkali, alkali-earth or rare-earth cations and B', B'' are typically W^{6+}, Mo^{6+} or other cations with tetrahedral coordination. Scheelites containing

rare-earth cations demonstrate luminescent properties and can be used in pc-WLEDs (phosphor-converted white-light-emitting-diode) [1–15].

Compounds with Eu^{3+} as luminescent centers produce intense red light. However, the application of these materials is hampered by the weak absorption strength of the parity forbidden $4f^6$-$4f^6$ transitions, which limits the excitation of Eu^{3+} with blue or near-UV light [16]. This problem can be partially alleviated by increasing the optical path length or by increasing the concentration of luminescent centers [17]. However, at high concentrations the internal quantum efficiency decreases owing to the energy transfer to non-radiative defect centers, i.e. so-called concentration quenching. In this regard, the local coordination environment of the Eu^{3+} species can play an important role in the performance of the material, because it can affect the excitation energy transfer.

Cation ordering is one of the prominent factors controlling the local coordination environment of the A cations, and thus that of Eu^{3+}. However, in stoichiometric scheelites (a = b in the formula), ordering between the A'/A'' cations is rare. Typically, it is realized when the ionic radius of A' is about 0.35 Å larger than that of A'', provided that the A' cation has a formal charge larger than that of A'' [18–24]. On the other hand, scheelite-based materials can accommodate a large amount of vacancies in the A sublattice (compounds with a < b) [25–29] In these structures, A'/A'' cation ordering is more common, because it is also coupled to the ordering between cations and vacancies; and can occur for the A'/A'' ionic radii differences as low as ~ 0.1 Å. Typically this results in the formation of incommensurately modulated structures with pronounced occupational modulation [27,29].

Recently we investigated a $CaGd_{2(1-x)}Eu_{2x}\square(MoO_4)_{4(1-y)}(WO_4)_{4y}$ ($0 \le x \le 1$, $0 \le y \le 1$) family of cation deficient scheelites [18,30,31]. These materials emit intense red light dominated by the $^5D_0$–$^7F_2$ transition at 612 nm and demonstrate excellent performance as thermographic phosphors. The cation-vacancy ordering in these compounds results in incommensurately

modulated structures. Although Eu is slightly larger than Gd, the substitution of Eu^{3+} for Gd^{3+} does not affect the nature of the modulation, whereas the replacement of W^{6+} by Mo^{6+} with very similar ionic radii changes the modulation from (3+1)D to (3+2)D. The observed changes in the luminescent properties with the changing composition could not be directly related to the structure of the materials, because the increasing concentration of Eu^{3+} increases the contribution of non-radiative decay paths (concentration quenching). Therefore, in the present study we investigate the effect of cation vacancies on the crystal structure and luminescent properties of Eu^{3+} containing scheelites. Using $Ca_{0.85-1.5x}Gd_xEu_{0.1}\square_{0.05+0.5x}WO_4$ ($0 \leq x \leq 0.567$) materials, we vary the vacancy concentration by the heterovalent substitution of Ca^{2+} by Gd^{3+}, while keeping the Eu^{3+} concentration constant.

2. Experimental section

Samples of $Ca_{0.85-1.5x}Gd_xEu_{0.1}\square_{0.05+0.5x}WO_4$ (x = 0, 0.1, 0.2, 0.3, 0.4, and 0.567) were synthesized by a solid state reaction from a stoichiometric mixture of $CaCO_3$, Gd_2O_3, Eu_2O_3 and WO_3 (99.99%) at 823 K for 10 h followed by annealing at 1273 K for 96 h.

Laboratory X-ray powder diffraction (XRD) was used for monitoring the completeness of the reaction and for preliminary analysis of the evolution of the $Ca_{0.85-1.5x}Gd_xEu_{0.1}\square_{0.05+0.5x}WO_4$ ($0 \leq x \leq 0.567$) structures with x. The data were collected on a Huber G670 Guinier diffractometer ($CuK\alpha_1$ radiation, curved Ge(111) monochromator, transmission mode, image plate).

High-resolution synchrotron X-ray powder diffraction (SXPD) data for the crystal structure refinement were collected at 300 K at the ID22 (former ID31) beamline of the European Synchrotron Radiation Facility (ESRF, Grenoble) at wavelength λ = 0.39996 Å in the 2θ range 1−40°. The powder sample was thoroughly ground and placed in a thin-walled borosilicate glass capillary of about 0.3 mm in diameter, which was spun

during the experiments. The crystal structures were refined using the Rietveld method. All crystallographic analyses were done in the JANA2006 package [32].

Samples for electron microscopy were prepared by grinding the powder in a mortar under ethanol and putting a few drops of the dispersion onto holey carbon TEM grids. Selected area electron diffraction (ED) patterns were recorded on a Philips CM20 transmission electron microscope operated at 200 kV. Dark field TEM images and high resolution TEM images were recorded on an FEI Tecnai Osiris microscope operated at 200 kV. High angle annular dark field scanning transmission electron microscopy (HAADF-STEM) images were acquired on a probe aberration corrected FEI Titan^3 80-300 at 300 kV.

Luminescence emission and excitation spectra were obtained with a FS920 spectrometer (Edinburgh Instruments), using a 450 W xenon light source, double excitation monochromator and a R928P photomultiplier connected to the emission monochromator. Photoluminescence spectra of all samples were measured under the same conditions. The measurements were performed at room temperature unless stated otherwise and corrected for the sensitivity of the spectrometer. Decay profiles were collected using an Andor intensified CCD (Andor DH720) connected to a 500 mm spectrograph, combined with a dye laser as excitation source. Temperature dependent measurements were performed using an Oxford Optistat CF cryostat.

3. Results

3.1. Preliminary characterization

The most intense peaks in the XRD patterns of the $Ca_{0.85-1.5x}Gd_xEu_{0.1}\square_{0.05+0.5x}WO_4$ materials with $0 \leq x \leq 0.3$ (Fig. 1) are associated with a body-centered tetragonal scheelite-type lattice (*S.G.* $I4_1/a$). At $x = 0.4$, the *hkl*, *h*0*l* and *h*00

reflections split, indicating the monoclinic distortion of the basic scheelite-type structure. The most pronounced splitting occurs for the 112 reflection (bottom right panel in Fig. 1). Besides, weaker satellite reflections appear in the XRD patterns for $x = 0.3$ and 0.4 (marked with stars in the bottom left panel in Fig. 1). These reflections are attributed to cation-vacancy ordering and the formation of modulated structures [20,22,26,28–30]. Further increase of the Gd^{3+} content up to $x = 0.567$ ($Gd_{0.567}Eu_{0.1}\square_{0.05+0.5x}WO_4$) leads to the formation of a monoclinic phase (*S.G.* C2/*c*) with the $Eu_{2/3}WO_4$-type structure. Interestingly, up to $x = 0.3$ the increasing concentration of the cation vacancies due to the substitution of Gd^{3+} for Ca^{2+} increases the unit cell volume of the scheelite sublattice (Table S1 of Supporting Information) despite the fact that the ionic radius of Gd^{3+} (r = 1.053 Å, CN = 8) is smaller than that of Ca^{2+} (r = 1.12 Å, CN = 8) [33].

3.2. TEM study

Typically, occupational modulations in scheelite-based structures are confined to the *ab* planes, so that the ED taken along the [001] zone axis are the most informative [20,22,26,28–30]. The [001] ED patterns of the $Ca_{0.85-1.5x}Gd_xEu_{0.1}\square_{0.05+0.5x}WO_4$ compounds are shown in Fig. 2. The strong reflections are attributed to the basic scheelite sublattice and their position is similar in all [001] patterns for the different *x* values. On the other hand, the presence and positions of the satellite reflections depend on *x*.

The ED pattern of $Ca_{0.7}Gd_{0.1}Eu_{0.1}\square_{0.1}WO_4$ ($x = 0.1$) can be completely indexed using a tetragonal scheelite structure with the $I4_1/a$ space group and unit cell parameters $a \approx 5.25$ Å and $c \approx 11.40$ Å. The absence of the satellite reflections indicates a random distribution of Ca, Gd, Eu and cation vacancies in this structure.

The ED pattern of $Ca_{0.4}Gd_{0.3}Eu_{0.1}\square_{0.2}WO_4$ (x = 0.3) is very similar to those reported for $Na_{2/7}Gd_{4/7}MoO_4$ and $CaEu_2(MoO_4)_4$ with (3+2)D incommensurately modulated structures [28,30]. Indexing of the pattern requires five *hklmn* indexes given by the diffraction vector $\mathbf{H} = h\mathbf{a}^* + k\mathbf{b}^* + l\mathbf{c}^* + m\mathbf{q_1} + n\mathbf{q_2}$, where $\mathbf{a}^*$, $\mathbf{b}^*$ and $\mathbf{c}^*$ are the reciprocal vectors of the basic scheelite structure and vectors $\mathbf{q_1} \approx 0.52\mathbf{a}^* + 0.81\mathbf{b}^*$ and $\mathbf{q_2} \approx -0.81\mathbf{a}^* + 0.52\mathbf{b}^*$ are two modulation vectors. The $\mathbf{q}_1$ and $\mathbf{q}_2$ vectors are symmetrically dependent according to the tetragonal symmetry of the underlying basic scheelite structure. The *hklmn*: $h + k + l$ = 2n and *hk*0*mn*: h, k = 2n reflection conditions are in agreement with the space group $I4_1/a$ for the basic structure. The absence of reflection conditions on the *m* and *n* indexes suggests the (3+2)D superspace group $I4_1/a(\alpha,\beta,0)00(-\beta,\alpha,0)00$ (88.2.59.1 in the Stokes - Campbell - van Smaalen notations) [34].

The $Ca_{0.55}Gd_{0.2}Eu_{0.1}\square_{0.15}WO_4$ (x = 0.2) [001] ED pattern demonstrates the same type of the satellite reflections. However, their intensity is much weaker than those in the $Ca_{0.4}Gd_{0.3}Eu_{0.1}\square_{0.2}WO_4$ (x = 0.3) structure. These reflections are not visible in the laboratory XRD (Fig. 1) nor in the SXPD patterns (see below). A similar discrepancy between ED and XRD data was observed earlier for $Na_{0.286}Eu_{0.571}\square_{0.143}MoO_4$ with a (3+2)D incommensurately modulated structure [29].

According to the XRD data, the $Ca_{0.25}Gd_{0.4}Eu_{0.1}\square_{0.25}WO_4$ (x = 0.4) material has a monoclinic distortion of the scheelite sublattice. Most reflections in the [001] ED pattern can be indexed using a diffraction vector $\mathbf{H} = h\mathbf{a}^* + k\mathbf{b}^* + l\mathbf{c}^* + m\mathbf{q}$ with a modulation vector $\mathbf{q} \approx 0.54\mathbf{a}^* + 0.79\mathbf{b}^*$ [20,22,26,29,30]. The reflection conditions *hklm*: $h + k + l$ = 2n and *hk*0*m*: h, k =2n suggest the (3+1)D monoclinic superspace group $I2/b(\alpha,\beta,0)00$ (15.1.4.1 in the Stokes-Campbell-van Smaalen notations; $B2/b(\alpha,\beta,0)00$ in a standard setting) [34]. However, one can notice that some weak reflections in the [001] ED pattern cannot be indexed using the chosen modulation vector. They correspond to a modulation

vector **q'** ≈ -0.79**a*** + 0.54**b***. The brightness of the satellite reflections attributed to the vectors **q** and **q'** varies depending on which part of the crystal is selected for the ED. This is clearly visualized using dark field (DF) TEM data (Fig. 3). Fig. 3a demonstrates the ED pattern taken from the entire crystal (Fig. 3b). Selecting first order satellite reflections attributed to the different modulation vectors highlights two distinct parts of the crystal (Figs. 3c and 3d). This indicates that the crystal consists of two large domains sharing the same basic scheelite sublattice, but having a different orientation of the modulation waves, which are nearly perpendicular to each other. The orientation of the boundary between the domains is close to the {100} plane. Although many crystals demonstrate segmentation into twin-related domains, weak satellites due to the **q'** vector are still present in single domain particles. This indicates the presence of very fine nano-sized domains inside the large grains, which can be directly visualized using high resolution HAADF-STEM and TEM images (Fig.4 and Fig. S2 of Supporting Information, respectively). The same type of twinned domains with a rotation of the modulation direction for 90° about the *c* axis are also found in other scheelites, such as $Na_{0.138}Eu_{0.621}MoO_4$ [29].

The HAADF-STEM images for $Ca_{0.85-1.5x}Gd_xEu_{0.1}\square_{0.05+0.5x}WO_4$ with x = 0.2, 0.3, and 0.4 taken along the [001] direction are shown in Fig. 4. The images consist of a square pattern of bright dots corresponding to the projected cation columns. In the scheelite structure, the A and B cation positions alternate along the *c* axis, so that in the [001] images they are projected on top of each other. The occupational modulations for these materials appear as stripes of cation columns with lower intensity (due to cation vacancies). To improve the visibility of the modulation, the HAADF-STEM images in Fig. 4 are shown after a soft Gaussian blur, the unfiltered experimental images are provided in Fig. S1 of Supporting Information. The modulation stripes in

$Ca_{0.55}Gd_{0.2}Eu_{0.1}\square_{0.15}WO_4$ (x = 0.2) are very weak and difficult to distinguish. Note that the corresponding satellite reflections on the ED pattern are also very weak (Fig. 2). On the HAADF-STEM image of $Ca_{0.4}Gd_{0.3}Eu_{0.1}\square_{0.2}WO_4$ (x = 0.3), the modulations are more pronounced. Consistently with the tetragonal (3+2)D symmetry they appear as a crisscross pattern of stripes of darker spots. On the HAADF-STEM image of the x = 0.4 compound, the stripes go along one direction in agreement with its (3+1)D monoclinic symmetry. However, in some parts of the crystals there are very small domains of a few nanometers, where the stripes are rotated over 90° with respect to the rest of the crystal. Such nano-size twin domains are also visible on the high resolution TEM images (Fig. S2 of Supporting Information) and they give rise to the extra reflections on the ED patterns (marked with **q**' in Fig. 2).

3.3. Crystal structure refinement

The crystal structure of the $Ca_{0.85-1.5x}Gd_xEu_{0.1}\square_{0.05+0.5x}WO_4$ materials (x = 0.1-0.4) was refined using SXPD data. The SXPD patterns of the x = 0.1 and 0.2 compounds contain reflections from the basic scheelite lattice only. Therefore these structures were refined in the $I4_1/a$ space group with random distribution of cation vacancies and $Ca^{2+}/Gd^{3+}/Eu^{3+}$ cations.

The SXPD patterns of $Ca_{0.4}Gd_{0.3}Eu_{0.1}\square_{0.2}WO_4$ (x = 0.3) and $Ca_{0.25}Gd_{0.4}Eu_{0.1}\square_{0.25}WO_4$ (x = 0.4) contain weak satellite reflections due to the cation ordering. Consistently with the ED data, the SXPD pattern of $Ca_{0.4}Gd_{0.3}Eu_{0.1}\square_{0.2}WO_4$ (x = 0.3) can be indexed with a (3+2)D modulated structure with a tetragonal superspace group $I4_1/a(\alpha,\beta,0)00(-\beta,\alpha,0)00$, with basic cell parameters close to those of the parent scheelite structure and two modulation vectors $\mathbf{q}_1$ = 0.51637(14)**a*** + 0.80761(13)**b*** and $\mathbf{q}_2$ = -0.80761(13)**a*** + 0.51637(14)**b***. The crystal structure refinement of this material

was performed using the structure model of $CaEu_2(MoO_4)_4$ [18]. The SXPD pattern of $Ca_{0.25}Gd_{0.4}Eu_{0.1}\square_{0.25}WO_4$ (x = 0.4) can be completely indexed using a (3+1)D scheelite-based monoclinic structure with a space group $I2/b(\alpha,\beta,0)00$ and the modulation vector $\mathbf{q}$ = 0.54206(8)$\mathbf{a}^*$ + 0.79330(8)$\mathbf{b}^*$. This structure was refined using the $CaEu_2(WO_4)_4$ structure as a starting model [18].

Despite apparent differences, the refinement of the x = 0.3 and x = 0.4 structures was quite similar. In both cases, only the first order satellite reflections are observed. For x = 0.3 the *hklmn* satellites with both $|m| \geq 1$ and $|n| \geq 1$ are almost invisible (the two most "prominent" reflections $101\bar{1}1$ and $200\bar{1}1$ have a relative intensity <0.04%). So, in the refinement we considered only the modulation waves corresponding to $|m| = 1$, $|n| = 0$ and $|m| = 0$, $|n| = 1$ for the x = 0.3 structure and $|m| = 1$ for the x = 0.4 structure.

The occupancy modulation of the A cations was refined using first order harmonic functions, i.e. in the form $p^{\lambda} = p_0^{\lambda} + p_1^{\lambda}\cos(2\pi x_4) + p_1^{\lambda}\cos(2\pi x_5)$ for the (3+2)D x = 0.3 structure and in the form $p^{\lambda} = p_0^{\lambda} + p_1^{\lambda}\cos(2\pi x_4)$ for the (3+1)D x = 0.4 structure, where p_0^{λ} represents the average concentration of a cation λ and p_1^{λ} is the modulation amplitude. The A positions in the structures are occupied by atomic species with three distinct scattering powers: Ca^{2+} cations, rare-earth cations and cation vacancies. Therefore, there are infinite possibilities to combine these species to produce the same total scattering density. To establish the distribution of the elements we used the procedure introduced by Abakumov *et al* [18]. First, the modulation of the total scattering density was refined using effective atomic species with the atomic number corresponding to the average atomic number of the cations occupying the A positions. Then, the admissible combinations of the p_1^{λ} amplitudes for Ca^{2+} and rare-earth cations were determined and certain values were accepted for further refinement. The details of this procedure are provided in Supporting Information.

In both the x = 0.3 and 0.4 structures, the displacive modulation was fitted with first order harmonic functions, since only the satellites of the first order were observed on the SXPD patterns. Parameters of the modulation functions that did not exceed their standard deviations were fixed to 0 in the refinement. Identical atomic coordinates and atomic displacement parameters (ADPs) were refined for the Ca, Gd and Eu atoms.

The experimental, calculated, and difference SXPD profiles after the Rietveld refinement are shown in Fig. 5. The crystallographic information is given in Table 1; the atomic parameters, coefficients of the modulation functions and main interatomic distances are given in Supporting Information, Tables S2-S7.

3.4. Luminescent properties

Fig. 6 demonstrates the room temperature excitation (top; λ_{em} = 615 nm) and emission (bottom; λ_{exc} = 395 nm) spectra for $Ca_{0.85-1.5x}Gd_xEu_{0.1}\square_{0.05+0.5x}WO_4$ (x = 0.1 - 0.567). The excitation spectra consists of a broad band in the low wavelength region, which can be assigned to the charge-transfer state (250-310 nm) and Eu^{3+} $4f^6$-$4f^6$ transitions between 300 and 400 nm [35]. Direct excitation of the $^5L_6$ level at 395 nm produces the emission spectra demonstrated in the bottom of Fig. 6. The displayed range contains the $^5D_2$-^7F_J (blue), $^5D_1$-^7F_J (green-yellow) and $^5D_0$-^7F_J ($^5D_0$-$^7F_0$ at λ_{em} = 579 nm; $^5D_0$-$^7F_1$ at λ_{em} = 590 nm and $^5D_0$-$^7F_2$ at λ_{em} = 615 nm) transitions. The $^5D_0$-$^7F_2$ induced electric dipole transition is the most intense due to the absence of an inversion center at the Eu^{3+} site [36].

Fig. 7 shows the intensity decay of the emission from the $^5D_1$ (monitored at 530-545 nm) and $^5D_0$ (monitored at 605-625 nm) levels after the excitation of the $^5L_6$ level at 395 nm. Both decay profiles can be fitted using monoexponential functions with the corresponding decay constants τ = 10 μs ($^5D_1$ emission) and τ = 550 μs ($^5D_0$ emission).

During the first few microseconds, the profiles deviate from the fitted model. The origin of this effect will be discussed below.

4. Discussion

The heterovalent substitution of Gd^{3+} and Eu^{3+} for Ca^{2+} in $CaWO_4$ gives rise to the $Ca_{0.85-1.5x}Gd_xEu_{0.1}\square_{0.05+0.5x}WO_4$ $(0 \leq x \leq 0.567)$ series of cation deficient scheelite structures. At low concentration (x = 0.1) the A cation vacancies are randomly distributed and the structures preserve the $I4_1/a$ symmetry. As the concentration of the vacancies increases, they tend to form an ordered distribution with the cations. At x = 0.2, the ordering can only be observed on a local scale, so that on average the structure retains the tetragonal symmetry with random distribution of the vacancies. At higher concentrations, long-range ordering between the cations and the cation vacancies sets in. At x = 0.3 it produces a (3+2)D tetragonal structure with two perpendicular modulation waves. Then, at x = 0.4 it gives rise to the (3+1)D monoclinic structure with a single modulation wave. This structure also contains nanodomains with 90° rotation of the modulation with respect to the rest of the crystal. Apparently they are formed as a result of the very small monoclinic distortion of the basic scheelite structure. Representative fragments of $Ca_{0.4}Gd_{0.3}Eu_{0.1}\square_{0.2}WO_4$ (x = 0.3) and $Ca_{0.25}Gd_{0.4}Eu_{0.1}\square_{0.25}WO_4$ (x = 0.4) are shown in Fig. 8. For clarity, they are represented as a single atomic layer along the z-axis. The images demonstrate the modulated occupancy of the A cations and the significant distortion of the WO_4 tetrahedra in both structures.

In order to analyze the details of the refined modulated structures, we plot the variations of several structural parameters (i.e. occupancy of the A sublattice, A−O and W−O bond lengths, tetrahedral distortion parameters) as t-u-plots for the $Ca_{0.4}Gd_{0.3}Eu_{0.1}\square_{0.2}WO_4$ (x = 0.3) structure and as t-plots for the

$Ca_{0.25}Gd_{0.4}Eu_{0.1}\square_{0.25}WO_4$ (x = 0.4) structure, which are shown in Figs. 9 and 10, respectively. The t and u parameters are the so-called internal coordinates of the modulated structure. They vary from 0 to 1 and account for all possible configurations of the modulated structure in the 3D physical space.

The structural parameters in both x = 0.3 and x = 0.4 compounds vary in a very similar way. The Ca and (Gd,Eu) occupational modulation waves are in antiphase relationship with the corresponding maxima at t = 1/2, u = 1/2 and t = 0, u = 0 in the x = 0.3 structure and $t \approx 0$ and $t \approx 1/2$ in the x = 0.4 structure (Fig. 9a,b and 10a,b). This behavior indicates that the ordering between cations and the cation vacancies also induces partial ordering between the Ca and (Gd,Eu) species.

The AO_8 polyhedra are significantly distorted: in $Ca_{0.4}Gd_{0.3}Eu_{0.1}\square_{0.2}WO_4$ the A−O distances vary in the 2.23-2.75 Å range; in $Ca_{0.25}Gd_{0.4}Eu_{0.1}\square_{0.25}WO_4$ in the 2.36-2.61 Å range (Figs. 9c and 10c). The A−O bond lengths are shortest in the unit cells with the highest Gd+Eu occupancy and longest in the unit cells populated by Ca and vacancies. The deformation of the WO_4 tetrahedra can be analyzed using the W−O distances, O−W−O angles and the distortion parameters Δd and $\Delta\alpha$. In $Ca_{0.4}Gd_{0.3}Eu_{0.1}\square_{0.2}WO_4$ (x = 0.3), the W−O distances are 1.59-1.95 Å; the O−W−O angles significantly deviate from the ideal tetrahedral angle of 109.5°, varying in a range 101-127°. In $Ca_{0.25}Gd_{0.4}Eu_{0.1}\square_{0.25}WO_4$ (x = 0.4), the tetrahedra are slightly less distorted with W−O varying between 1.72-1.84 Å and O−W−O angles 104-124°. The distortion parameters Δd and $\Delta\alpha$ characterize the deviations of the W−O bond length from the average value (d) and the deviations of the O−W−O bond angles from the perfect tetrahedral angle (α = 109.5°):

$$\Delta d = 1/4 \sum_{n=1-4} \left[\frac{d_n - d}{d}\right]^2 \quad (1)$$

$$\Delta\alpha = 1/6 \sum_{n=1-6} \left[\frac{\alpha_n - \alpha}{\alpha}\right]^2 \quad (2)$$

where d_n is the individual W−O bond length, α_n is the individual O−W−O bond angle. The values of Δd and $\Delta\alpha$ also confirm that the distortion of the WO_4 tetrahedra in $Ca_{0.4}Gd_{0.3}Eu_{0.1}\square_{0.2}WO_4$ (max $\Delta d \approx 0.0051$; max $\Delta\alpha \approx 0.0057$) is larger than in $Ca_{0.25}Gd_{0.4}Eu_{0.1}\square_{0.25}WO_4$ (max $\Delta d \approx 0.0006$; max $\Delta\alpha \approx 0.0040$). However, the distortion patterns are slightly different in the structures. In $Ca_{0.25}Gd_{0.4}Eu_{0.1}\square_{0.25}WO_4$, the stretching and angular distortion modes demonstrate clear antiphase behavior, i.e. the minima of Δd occur in the same unit cells as the maxima of $\Delta\alpha$ (Fig. 10e,f). In $Ca_{0.4}Gd_{0.3}Eu_{0.1}\square_{0.2}WO_4$ ($x = 0.3$) some minima of Δd also coincide with the maxima of $\Delta\alpha$, but the maxima of Δd correspond to the unit cells with intermediate $\Delta\alpha$ values and at $t = 1/2$, $u = 1/2$ the minimum of Δd coincides with the minimum $\Delta\alpha$ (Fig. 9e,f).

Considering the luminescent properties of the materials, the decay profiles of the $^5D_0$ emission (Fig. 11) for all investigated samples are monoexponential with a decay constant τ of about 550 μs. Very similar decay times for different x reflect a similar internal quantum efficiency for all compounds. Apparently the changing structure does not significantly affect the involved energy transfer processes. During the first few μs after the excitation, the intensity of the emission coming from the $^5D_0$ level (Fig. 11, top) and $^5D_1$ level (Fig. 11, bottom) increases due to a continuous feeding from higher energy levels. The rise of the $^5D_1$ emission can be attributed to feeding from the $^5D_2$ level, because levels with even higher energy exhibit a decay too fast to be detected, presumably via multiphonon relaxation. As the time scale of the emission increases and the decays sufficiently differ from each other, the decay profile can be fitted with the following expression:

$$I(t) = I_1 \exp\left(-t/\tau_1\right) - I_2 \exp\left(-t/\tau_2\right) \quad (3)$$

where τ_1 = 10 μs and τ_2 = 1 μs [37]. The latter is of the same order as the decay component of the emission coming from the $^5D_2$ level (not shown), proving the feeding of the $^5D_1$ level via the $^5D_2$ level. For the emission coming from the $^5D_0$ level, two contributions can be distinguished during the initial increase, so an extra component has to be added, leading to:

$$I(t) = I_1 \exp\left(-t/\tau_1\right) - \left[I_2 \exp\left(-t/\tau_2\right) + I_3 \exp\left(-t/\tau_3\right)\right] \quad (4)$$

This approximation is only valid if $\tau_1 >> \tau_2, \tau_3$, which is indeed the case, as τ_1 = 550 μs, τ_2 = 6.5 μs and τ_3 = 1 μs. The decay component τ_3 here can again be linked to a feeding mechanism from the $^5D_2$ level, whereas τ_2 is the manifestation of the feeding from the $^5D_1$ level. Apparently, this demonstrates the partial relaxation from the $^5D_2$ to the $^5D_1$ level and subsequently to the $^5D_0$ level. The shapes of the decay profiles for different compounds in the $Ca_{0.85-1.5x}Gd_xEu_{0.1}\square_{0.05+0.5x}WO_4$ ($0 \leq x \leq 0.567$) series are identical and characteristic of isolated Eu^{3+} ions [38].

The cation-vacancy ordering in the $Ca_{0.85-1.5x}Gd_xEu_{0.1}\square_{0.05+0.5x}WO_4$ (x = 0.1 - 0.567) materials creates different coordination environments for the A cations. It does not significantly alter the $4f^6$-$4f^6$ transitions in the Eu^{3+} species. However, it affects the multiplet splitting of the initial emitting and final energy levels in the ^5D_J-$^7F_{J'}$ transitions [36]. Emission spectra due to the $^5D_0$-$^7F_2$ transition measured at room temperature and 10 K are shown in Fig. 12. The position and the linewidth of the spectral components systematically change with the increasing concentration of cation vacancies. These transformations are subtle for the compounds with x increasing from 0.1 to 0.4 and rather abrupt at x = 0.567.

The changes in the emission spectra can be correlated with the transformations of the Eu^{3+} coordination environment [39]. The x = 0.1 material adopts an ideal tetragonal scheelite structure with random distribution of Ca, (Eu,Gd) and cation vacancies. The

AO_8 polyhedra in this structure have the most symmetric configuration with two characteristic A-O distances of 2.431(2) Å and 2.482(3) Å. Increasing the vacancy concentration gives rise to an occupational modulation, which in turn results in the displacive modulation and the deformation of the AO_8 polyhedra. In the $x = 0.2$ material the modulations are very weak. They could only be detected on a local scale using TEM, while the XRD data is best described with the average tetragonal structure. In the $x = 0.3$ and 0.4 structures, the modulations are more pronounced. The intensity of the satellite reflections due to cation ordering gradually increases from $x = 0.2$ to $x = 0.4$. In these materials the deformation of the AO_8 polyhedra results in eight independent A-O distances. In the $x = 0.567$ structure the supercell reflections due to cation ordering are much stronger than the satellite reflections in $x = 0.3$ and 0.4 (Fig. 1). Since this material is isostructural to $Eu_{2/3}WO_4$, one can assume that the AO_8 polyhedra in this structure have very distinct geometry also with eight independent A-O distances, but they do not change across the structure.

Consistently with the described changes in the Eu^{3+} local coordination environment, the $^5D_0$-$^7F_2$ transitions demonstrate a gradual increase in the emission linewidth from $x = 0.1$ to 0.4, and then an abrupt decrease for $x = 0.567$. The $^5D_0$-$^7F_0$ transition typically demonstrates the smallest bandwidth of all occurring $4f^6$-$4f^6$ transitions due to the absence of multiplet splitting. The corresponding FWHMs change from 8 cm^{-1} for $x = 0.1$ to 9 cm^{-1} for $x = 0.2$ and 0.3, 12 cm^{-1} for $x = 0.4$ and finally to 5 cm^{-1} for $x = 0.567$. Also, the position and the splitting of the multiplet lines demonstrate that the AO_8 polyhedra transform gradually from $x = 0.1$ to 0.4 and then assume distinctly different configuration for $x = 0.567$.

Concluding remarks

In this work, we have unveiled the effect of the cation vacancies on the crystal structure of $Ca_{0.85-1.5x}Gd_xEu_{0.1}\square_{0.05+0.5x}WO_4$ ($0 \leq x \leq 0.567$) scheelite-based red phosphors and demonstrated that the changes in the local coordination environment of Eu^{3+} species correlate with the changes in the luminescent properties of the materials. In the $x = 0.1$ compound with the $I4_1/a$ symmetry, the cation vacancies are randomly distributed. The XRD data for the x = 0.2 structure also demonstrate random distribution of the vacancies, but the TEM data unveil local cation-vacancy ordering. As x increases, the ordering becomes more pronounced. At x = 0.3 and 0.4 it results in an incommensurately modulated structure. According to the structure refinement the cation-vacancy ordering in these materials also induces partial ordering between Ca^{2+} and rare-earth cations. Further increase of Gd^{3+} content to $x = 0.567$ results in a monoclinic phase (space group C2/c) with the $Eu_{2/3}WO_4$-type structure. The increasing concentration of the cation vacancies affects neither the luminescence decay lifetime nor the quantum efficiency of the materials. However, it changes the position and the linewidth of the emission spectra components by altering the AO_8 coordination polyhedra. Our results demonstrate that at low concentration of luminescent Eu^{3+} centers in the scheelite-based structures the cation-vacancy ordering and the local coordination of the species have a subtle effect on the luminescent properties. This further deepens the understanding of the structure-properties correlations, which can improve the design and industrial application of such light emitting materials.

Acknowledgements

This research was supported by FWO (project G039211N), Flanders Research Foundation. V.A.M. is grateful for financial support of the Russian Foundation for Basic

Research (Grant 15-03-07741). We are grateful to the ESRF for granting the beamtime at the ID22 beamline and to Andy Fitch for the support during the experiment.

References

[1] S. Neeraj, N. Kijima, A.K. Cheetham, Novel red phosphors for solid-state lighting: The system $NaM(WO_4)_{2-x}(MoO_4)_x:Eu^{3+}$ (M=Gd, Y, Bi), Chem. Phys. Lett. 387 (2004) 2–6.

[2] T. Kim, S. Kang, Potential red phosphor for UV-white LED device, J. Lumin. 122–123 (2007) 964–966.

[3] K. Hwang, Y. Jeon, S. Hwangbo, J. Kim, Red-emitting $LiEuW_2O_8$ phosphor for white emitting diodes prepared by sol–gel process, Opt. Appl. XXXIX (2009) 375–382.

[4] B. Yan, J.H. Wu, $NaY(MoO_4)_2:Eu^{3+}$ and $NaY_{0.9}Bi_{0.1}(MoO_4)_2:Eu^{3+}$ submicrometer phosphors: Hydrothermal synthesis assisted by room temperature-solid state reaction, microstructure and photoluminescence, Mater. Chem. Phys. 116 (2009) 67–71.

[5] M.M. Haque, H.I. Lee, D.K. Kim, Luminescent properties of Eu^{3+}-activated molybdate-based novel red-emitting phosphors for LEDs, J. Alloys Compd. 481 (2009) 792–796.

[6] Q. Shao, H. Li, K. Wu, Y. Dong, J. Jiang, Photoluminescence studies of red-emitting $NaEu(WO_4)_2$ as a near-UV or blue convertible phosphor, J. Lumin. 129 (2009) 879–883.

[7] L. Yi, L. Zhou, Z. Wang, J. Sun, F. Gong, W. Wan, et al., $KGd(MoO_4)_2:Eu^{3+}$ as a promising red phosphor for light-emitting diode application, Curr. Appl. Phys. 10 (2010) 208–213.

[8] X. He, M. Guan, Z. Li, T. Shang, N. Lian, Q. Zhou, Enhancement of Fluorescence from $BaMoO_4:Pr^{3+}$ Deep-Red-Emitting Phosphor via Codoping Li^+ and Na^+ Ions, J. Am. Ceram. Soc. 94 (2011) 2483–2488.

[9] Q. Li, J. Huang, D. Chen, A new Pr^{3+}-activated molybdate-based phosphor for application to white LEDs with blue excitation, Luminescence. 26 (2011) 349–355.

[10] Z. Wang, Y. Zhang, L. Xiong, X. Li, J. Guo, M. Gong, A potential red-emitting

phosphor with high color-purity for near-UV light emitting diodes, Curr. Appl. Phys. 12 (2012) 1084–1087.

[11] Y. Liu, Z.-G. Lu, Y.-Y. Gu, W. Li, Hydrothermal-assisted ion exchange synthesis and photoluminescence of Li^{+} and Eu^{3+} co-doped $NaLa(WO_4)_2$ as near-UV type red phosphors, J. Lumin. 132 (2012) 1220–1225.

[12] L. Qin, Y. Huang, T. Tsuboi, H.J. Seo, The red-emitting phosphors of Eu^{3+}-activated $MR_2(MoO_4)_4$ (M=Ba, Sr, Ca; R=La^{3+}, Gd^{3+}, Y^{3+}) for light emitting diodes, Mater. Res. Bull. 47 (2012) 4498–4502.

[13] A. Khanna, P.S. Dutta, Narrow spectral emission $CaMoO_4$: Eu^{3+}, Dy^{3+}, Tb^{3+} phosphor crystals for white light emitting diodes, J. Solid State Chem. 198 (2013) 93–100.

[14] L. Li, J. Zhang, W. Zi, S. Gan, G. Ji, H. Zou, et al., Synthesis and luminescent properties of high brightness $MRE(MoO_4)_2$:Eu^{3+} (M = Li, Na, K; RE = Gd, Y, Lu) red phosphors for white LEDs, Solid State Sci. 29 (2014) 58–65.

[15] Z. Wang, J. Zhong, H. Jiang, J. Wang, H. Liang, Controllable Synthesis of $NaLu(WO_4)_2$:Eu^{3+} Microcrystal and Luminescence Properties for LEDs, Cryst. Growth Des. 14 (2014) 3767–3773.

[16] P.F. Smet, A.B. Parmentier, D. Poelman, Selecting Conversion Phosphors for White Light-Emitting Diodes, J. Electrochem. Soc. 158 (2011) R37–R54.

[17] A. Katelnikovas, J. Plewa, S. Sakirzanovas, D. Dutczak, D. Enseling, F. Baur, et al., Synthesis and optical properties of $Li_3Ba_2La_3(MoO_4)_8$:Eu^{3+} powders and ceramics for pcLEDs, J. Mater. Chem. 22 (2012) 22126–22134.

[18] A.M. Abakumov, V.A. Morozov, A.A. Tsirlin, J. Verbeeck, J. Hadermann, Cation Ordering and Flexibility of the $BO_4^{(2-)}$ Tetrahedra in Incommensurately Modulated $CaEu_2(BO_4)_4$ (B = Mo, W) Scheelites., Inorg. Chem. 2 (2014) 2–10.

[19] J. Hanuza, A. Benzar, A. Haznar, M. Maczka, A. Pietraszko, J.H. van der Maas,

Structure and vibrational dynamics of tetragonal $NaBi(WO_4)_2$ scheelite crystal, Vib. Spectrosc. 12 (1996) 25–36.

[20] V.A. Morozov, A. V. Arakcheeva, G. Chapuis, N. Guiblin, M.D. Rossell, G. Van Tendeloo, $KNd(MoO_4)_2$: A new incommensurate modulated structure in the scheelite family, Chem. Mater. 18 (2006) 4075–4082.

[21] X. Han, A. García-Cortés, M.D. Serrano, C. Zaldo, C. Cascales, Structural and thermal properties of tetragonal double tungstate crystals intended for ytterbium laser composites, Chem. Mater. 19 (2007) 3002–3010.

[22] A. V. Arakcheeva, P. Pattison, G. Chapuis, M. Rossell, A. Filaretov, V. Morozov, et al., $KSm(MoO_4)_2$, an incommensurately modulated and partially disordered scheelite-like structure, Acta Crystallogr. Sect. B Struct. Sci. 64 (2008) 160–171.

[23] G.M. Kuz'micheva, V.B. Rybakov, V.L. Panyutin, E. V. Zharikov, K.A. Subbotin, Symmetry of $(Na_{0.5}R_{0.5})MO_4$ crystals (R = Gd, La; M = W, Mo), Russ. J. Inorg. Chem. 55 (2010) 1448–1453.

[24] I.C. Nogueira, L.S. Cavalcante, P.F.S. Pereira, M.M. de Jesus, J.M. Rivas Mercury, N.C. Batista, et al., Rietveld refinement, morphology and optical properties of $(Ba_{1-x}Sr_x)MoO_4$ crystals, J. Appl. Crystallogr. 46 (2013) 1434–1446.

[25] E. Lukacevic, A. Santoro, R. Roth, Neutron powder diffraction study of the structure of the compound $Li_{0.3125}La_{0.5625}MoO_4$, Solid State Ionics. 18–19 (1986) 922–928.

[26] V.A. Morozov, A. V. Mironov, B.I. Lazoryak, E.G. Khaikina, O.M. Basovich, M.D. Rossell, et al., $Ag_{1/8}Pr_{5/8}MoO_4$: An incommensurately modulated scheelite-type structure, J. Solid State Chem. 179 (2006) 1183–1191.

[27] A. Arakcheeva, D. Logvinovich, G. Chapuis, V. Morozov, S. V. Eliseeva, J.-C.G. Bünzli, et al., The luminescence of $Na_xEu^{3+}_{(2-x)/3}MoO_4$ scheelites depends on the number of Eu-clusters occurring in their incommensurately modulated structure, Chem. Sci. 3 (2012) 384–

390.

[28] V. Morozov, A. V. Arakcheeva, B. Redkin, V. Sinitsyn, S. Khasanov, E. Kudrenko, et al., $Na_{2/7}Gd_{4/7}MoO_4$: A modulated scheelite-type structure and conductivity properties, Inorg. Chem. 51 (2012) 5313–5324.

[29] V.A. Morozov, B.I. Lazoryak, S.Z. Shmurak, A.P. Kiselev, O.I. Lebedev, N. Gauquelin, et al., Influence of the Structure on the Properties of $Na_xEu_y(MoO_4)_z$ Red Phosphors, Chem. Mater. 26 (2014) 3238–3248.

[30] V.A. Morozov, A. Bertha, K.W. Meert, S. Van Rompaey, D. Batuk, G.T. Martinez, et al., Incommensurate Modulation and Luminescence in the $CaGd_{2(1-x)}Eu_{2x}(MoO_4)_{4(1-y)}(WO_4)_{4y}$ ($0 \leq x \leq 1$, $0 \leq y \leq 1$) Red Phosphors, Chem. Mater. 25 (2013) 4387–4395.

[31] K.W. Meert, V.A. Morozov, A.M. Abakumov, J. Hadermann, D. Poelman, P.F. Smet, Energy transfer in Eu^{3+} doped scheelites: use as thermographic phosphor, Opt. Express. 22 (2014) A961–A972.

[32] V. Petříček, M. Dušek, L. Palatinus, Crystallographic Computing System JANA2006: General features, Zeitschrift Für Krist. - Cryst. Mater. 229 (2014) 345–352.

[33] R.D. Shannon, Revised effective ionic radii and systematic studies of interatomic distances in halides and chalcogenides, Acta Crystallogr. Sect. A. 32 (1976) 751–767.

[34] S. Van Smaalen, B.J. Campbell, H.T. Stokes, Equivalence of superspace groups, Acta Crystallogr. Sect. A Found. Crystallogr. 69 (2013) 75–90.

[35] P. Boutinaud, E. Cavalli, Predicting metal-to-metal charge transfer in closed-shell transition metal oxides doped with Bi^{3+} or Pb^{2+}, Chem. Phys. Lett. 503 (2011) 239–243.

[36] P.A. Tanner, Some misconceptions concerning the electronic spectra of tri-positive europium and cerium, Chem. Soc. Rev. 42 (2013) 5090–5101.

[37] J. Zhong, H. Liang, Q. Su, J. Zhou, Y. Huang, Z. Gao, et al., Luminescence properties of $NaGd(PO_3)_4:Eu^{3+}$ and energy transfer from Gd^{3+} to Eu^{3+}, Appl. Phys. B. 98 (2010) 139–147.

[38] L.A. Riseberg, H.W. Moos, Multiphonon Orbit-Lattice Relaxation of Excited States of Rare-Earth Ions in Crystals, Phys. Rev. 174 (1968) 429–438.

[39] K. Binnemans, Interpretation of europium(III) spectra, Coord. Chem. Rev. 295 (2015) 1–45.

Figures

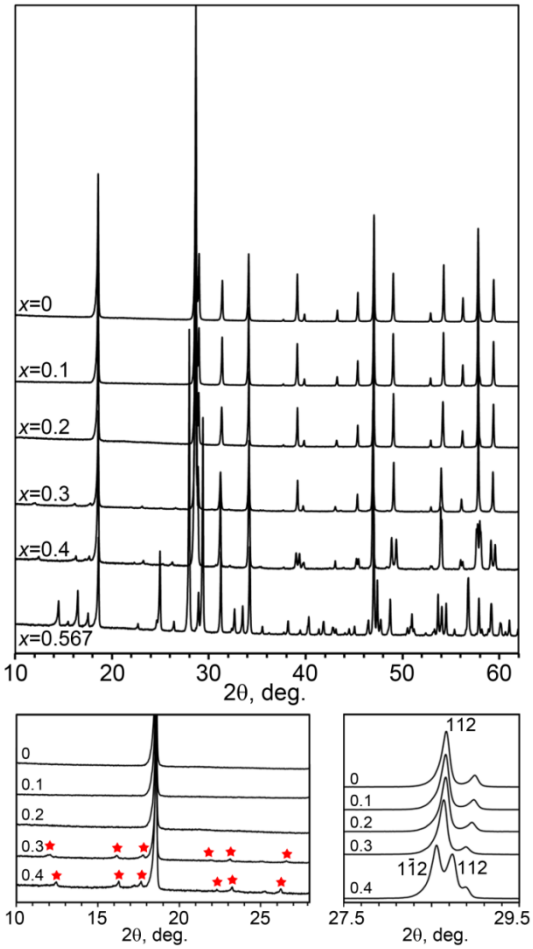

Fig. 1 XRD patterns of $Ca_{0.85-1.5x}Gd_xEu_{0.1}\square_{0.05+0.5x}WO_4$ compounds (x = 0, 0.1, 0.2, 0.3, 0.4, and 0.567). Weak satellite reflections due to A-site cation ordering can be observed in the 10°–28° 2θ range (bottom left, the reflections are marked with red stars). The enlarged 27.5°–29.5° 2θ range (bottom right) highlights the monoclinic splitting of the 112 reflection in the x = 0.4 sample.

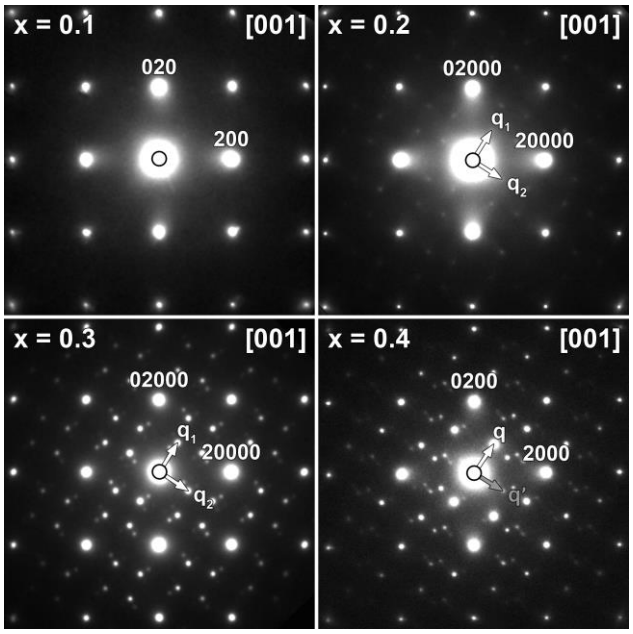

Fig. 2 [001] ED patterns of $Ca_{0.85-1.5x}Gd_xEu_{0.1}\square_{0.05+0.5x}WO_4$ (x = 0.1, 0.2, 0.3, and 0.4). The reflections on the x = 0.4 pattern corresponding to the q' vector originate from twin-related (nano-) domains (see text for more explanation).

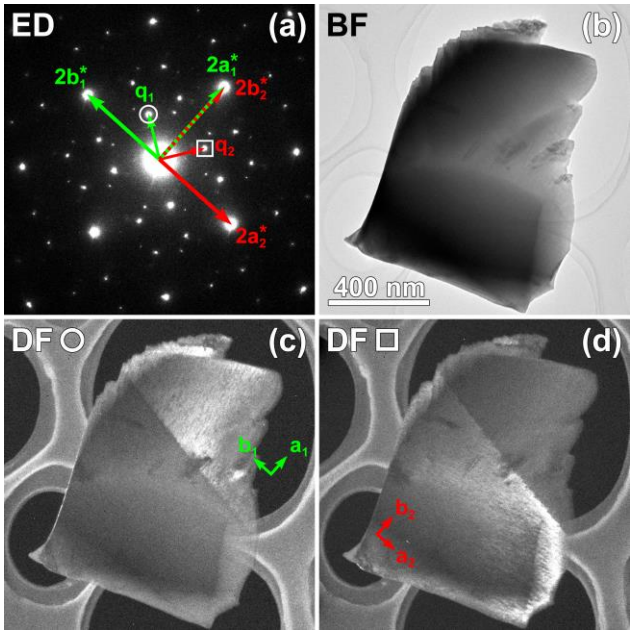

Fig. 3 (a) [001] ED pattern taken from a large crystal of $Ca_{0.25}Gd_{0.4}Eu_{0.1}\square_{0.25}WO_4$ (the bright field (BF) image of this crystal is shown in (b)). The circle and the square outline the reflections that were selected with the objective aperture to produce the corresponding dark field (DF) images in (c) and (d), respectively.

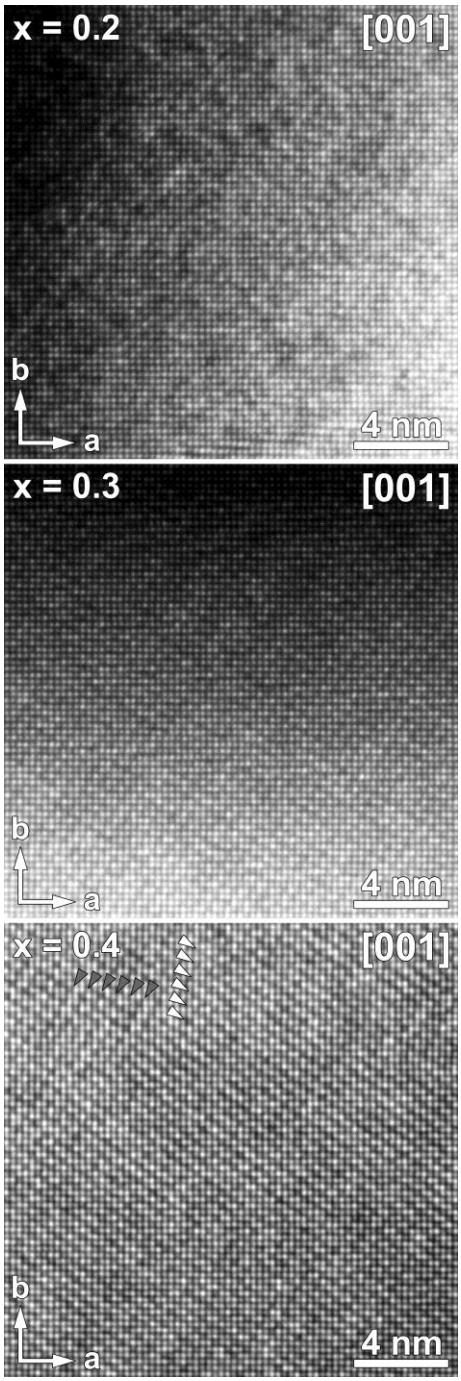

Fig. 4 [001] HAADF-STEM images of $Ca_{0.85-1.5x}Gd_xEu_{0.1}\square_{0.05+0.5x}WO_4$ (x = 0.2, 0.3, and 0.4) after smoothing using Gaussian filter. White arrowheads in the image for the x = 0.4 structure indicate the modulation stripes due to main modulation (vector **q**). Grey arrowheads highlight a nanodomain with the modulation rotated for 90° about the *c* axis.

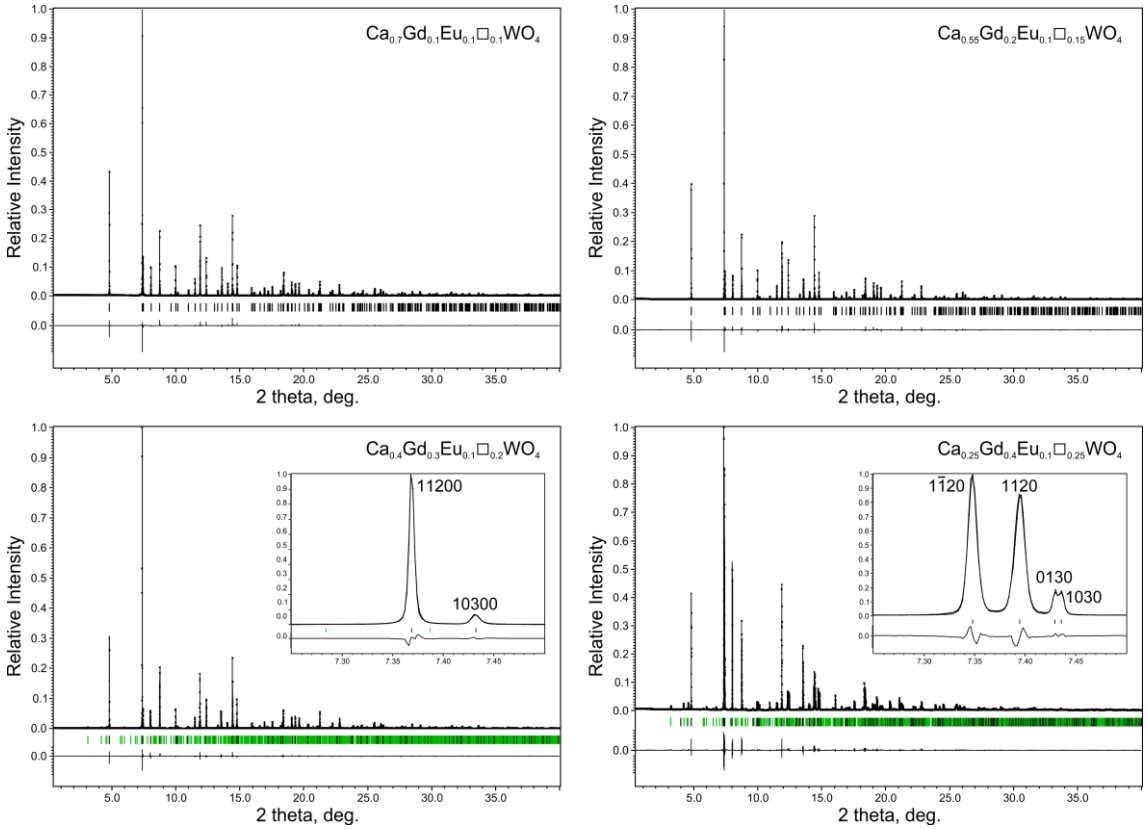

Fig. 5 Experimental, calculated, and difference SXPD profiles after Rietveld refinement of the $Ca_{0.85-1.5x}Gd_xEu_{0.1}\square_{0.05+0.5x}WO_4$ (x = 0.1-0.4) structures. The insets show the main reflections 112 and 103 in tetragonal $Ca_{0.4}Gd_{0.3}Eu_{0.1}\square_{0.2}WO_4$ and their splitting in monoclinic $Ca_{0.25}Gd_{0.4}Eu_{0.1}\square_{0.25}WO_4$. Black and green bars mark the positions of the main and satellite reflections, respectively.

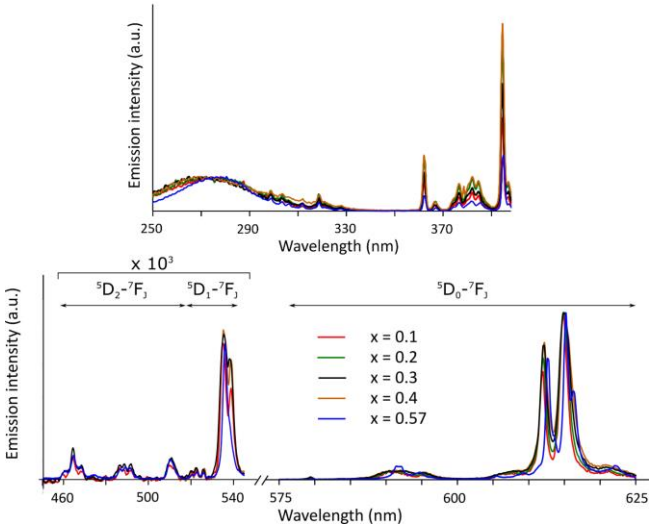

Fig. 6 Excitation (top; λ_{em} = 615 nm) and emission (bottom; λ_{exc} = 395 nm) spectra of $Ca_{0.85-1.5x}Gd_xEu_{0.1}\square_{0.05+0.5x}WO_4$ (x = 0.1 - 0.567).

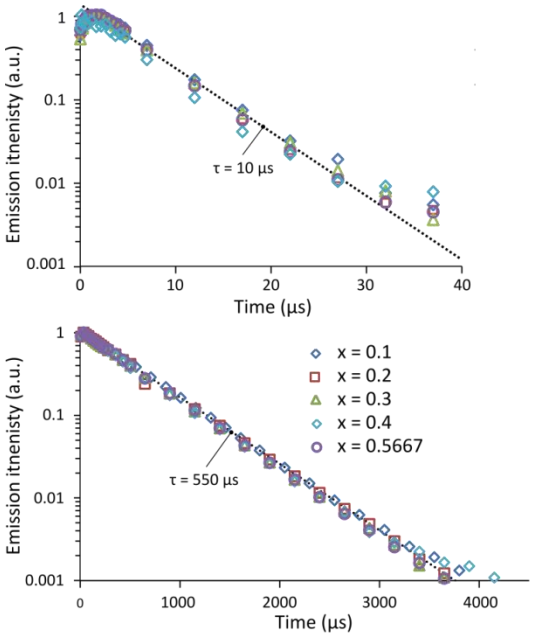

Fig. 7 Decay profiles of the emission intensity originating from the $^5D_1$ (top) and $^5D_0$ (bottom) levels (λ_{exc} = 395 nm) of $Ca_{0.85-1.5x}Gd_xEu_{0.1}\square_{0.05+0.5x}WO_4$ (x = 0.1, 0.2, 0.3, 0.4, 0.567).

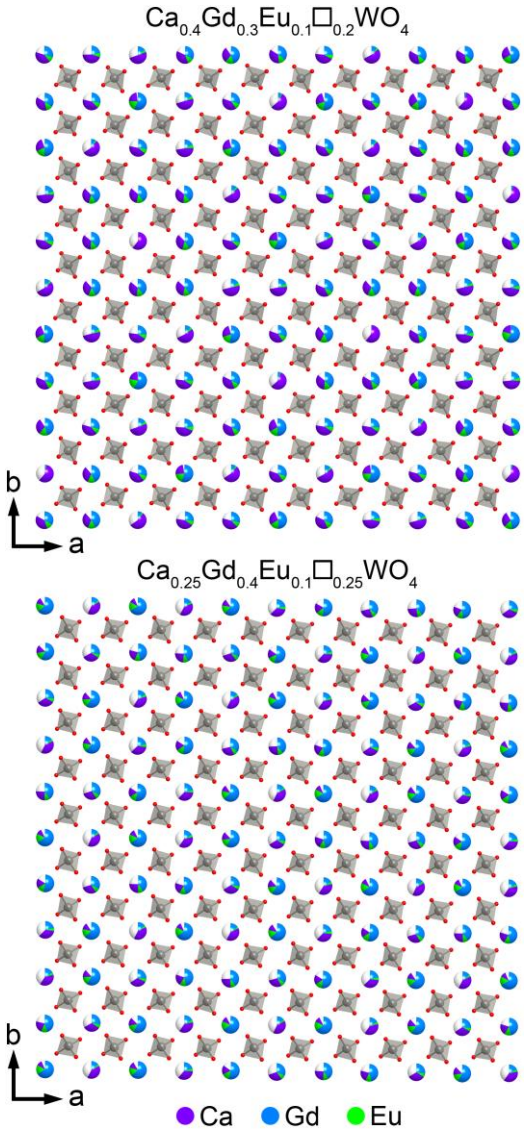

Fig. 8 One layer (along *c*) of a 10×10 supercell for the $Ca_{0.4}Gd_{0.3}Eu_{0.1}\square_{0.2}WO_4$ (x = 0.3) and $Ca_{0.25}Gd_{0.4}Eu_{0.1}\square_{0.25}WO_4$ (x = 0.4) structures. The occupancy of the *A*-sites is shown through colored sectors: violet for Ca, blue for Gd, green for Eu, and transparent for vacancies. The W atoms at the center of the tetrahedra are shown in grey. The O atoms are shown as red spheres.

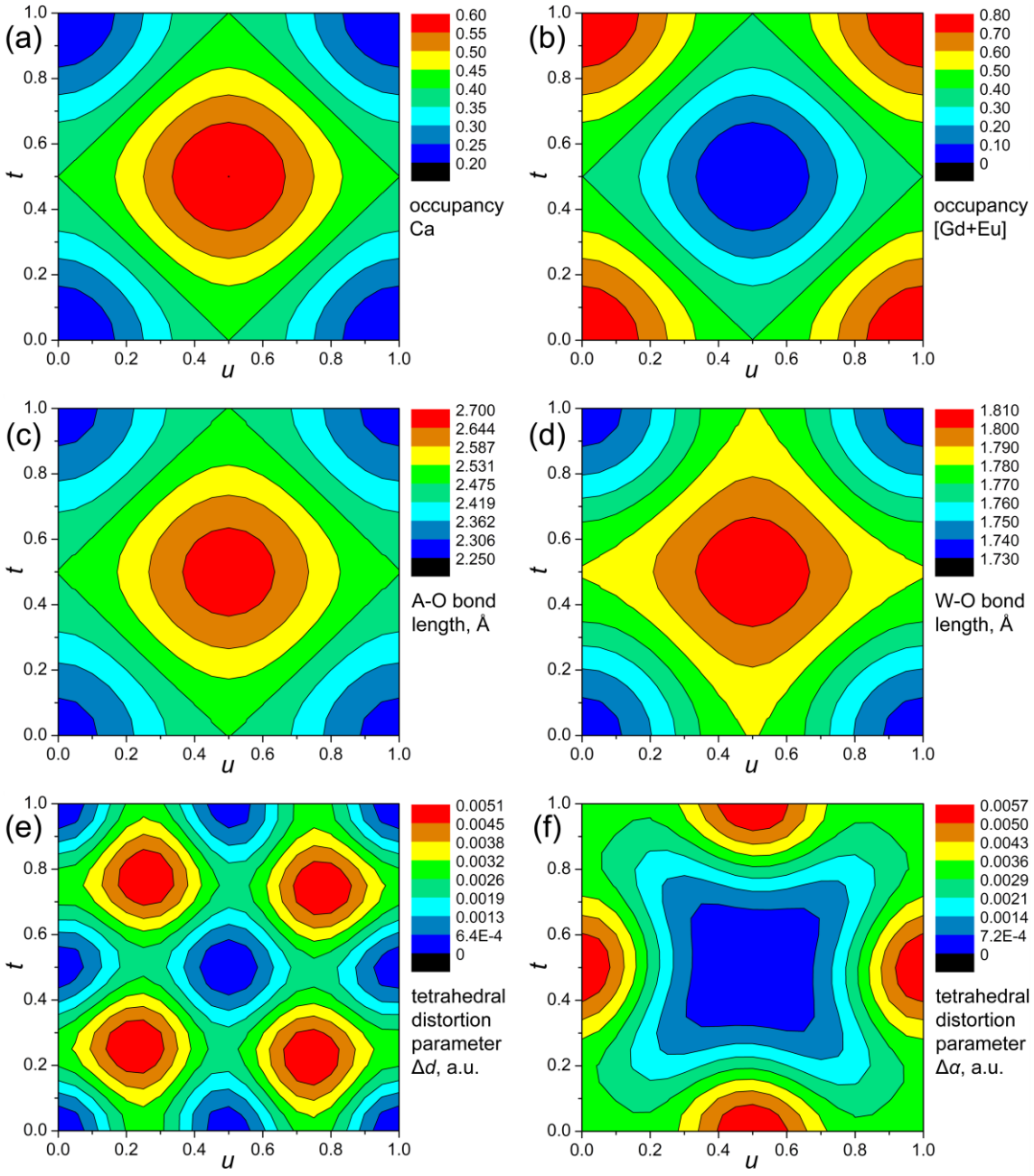

Fig. 9 *t*-*u*-plots for the $Ca_{0.4}Gd_{0.3}Eu_{0.1}\square_{0.2}WO_4$ structure: variation of the Ca occupancy (a); Gd+Eu occupancy (b); average A−O bond length (c); average W−O bond length (d); and tetrahedral distortion parameters Δd (e) and $\Delta\alpha$ (f).

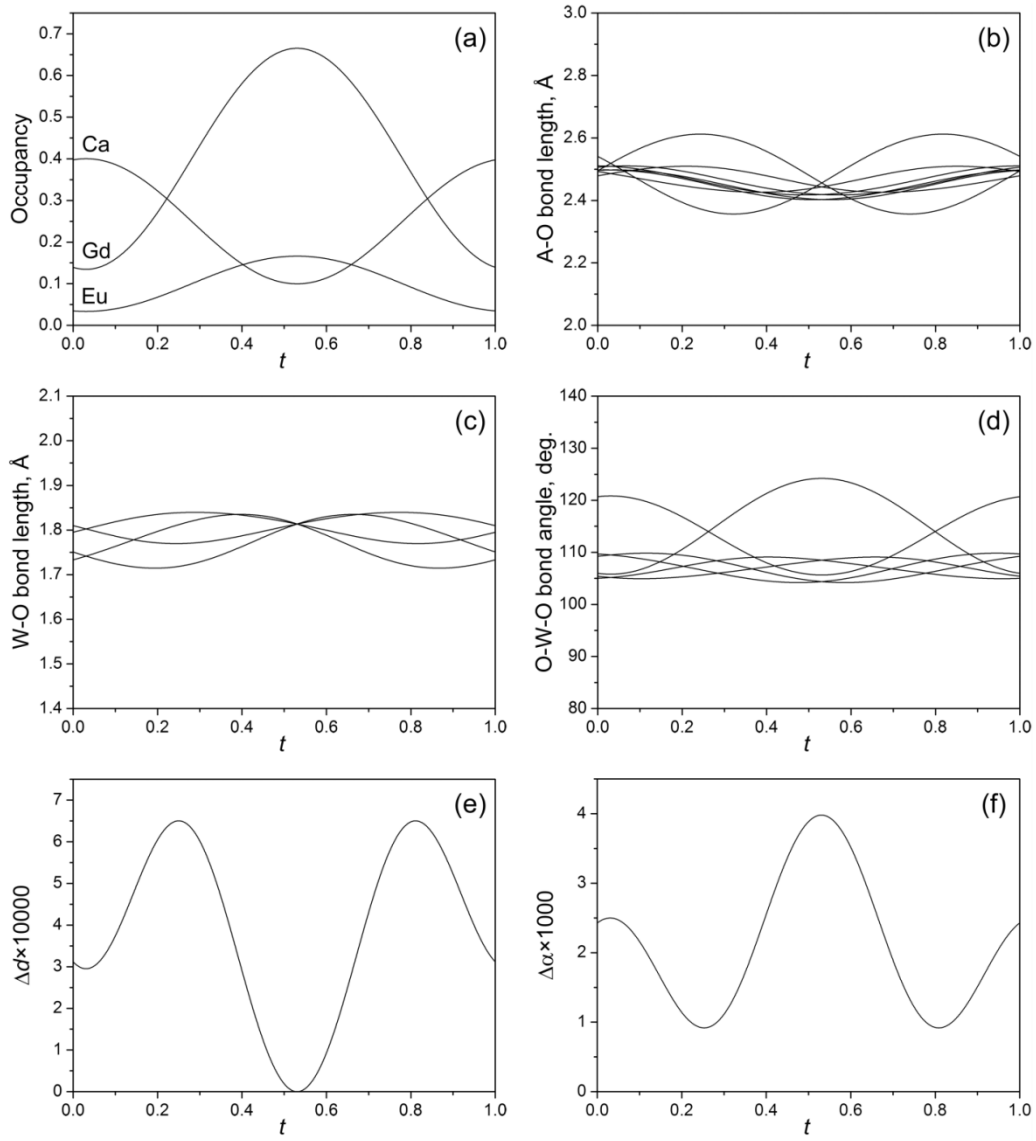

Fig. 10 *t*-plots for the $Ca_{0.25}Gd_{0.4}Eu_{0.1}\square_{0.25}WO_4$ structure: variation of the Ca/Gd/Eu occupancies (a); A−O bond length (b); W−O bond length (c); O−W−O bond angles (d); and tetrahedral distortion parameters Δd (e) and $\Delta\alpha$ (f).

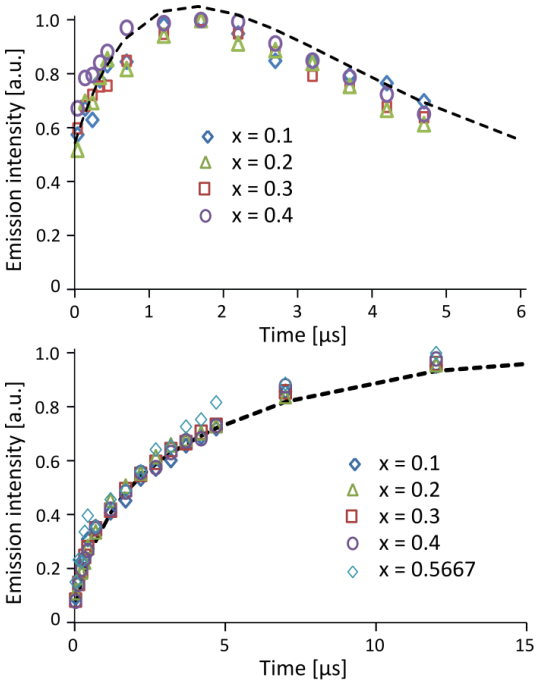

Fig. 11 Decay profile (λ_{exc} = 395 nm) of the $^5D_1$ (λ_{em} = 530 – 545 nm, top) and $^5D_0$ (λ_{em} = 605-625 nm, bottom) emission. The dashed line is the fit to the experimental data (see text for more details).

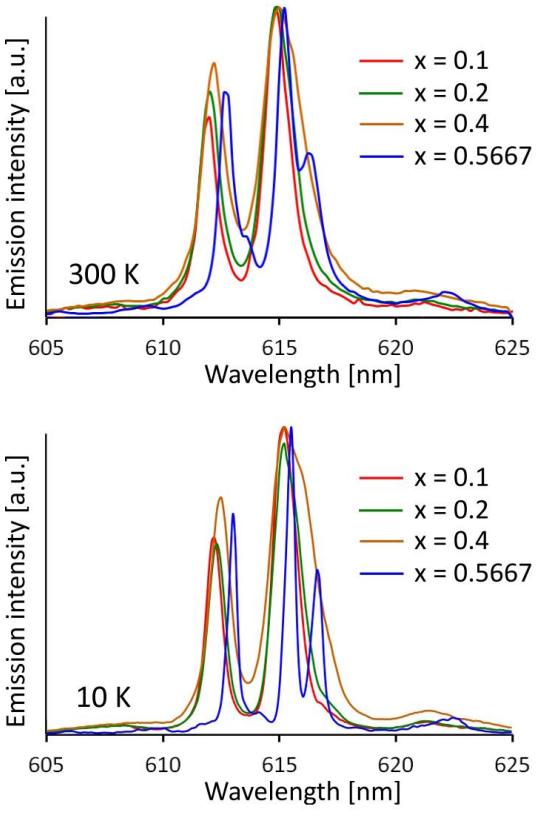

Fig. 12 The $^5D_0$-$^7F_2$ transition (λ_{exc} = 395 nm) of $Ca_{0.85-1.5x}Gd_xEu_{0.1}\square_{0.05+0.5x}WO_4$ (x = 0.1, 0.2, 0.4 and 0.567) at room temperature (top) and at 10 K (bottom).